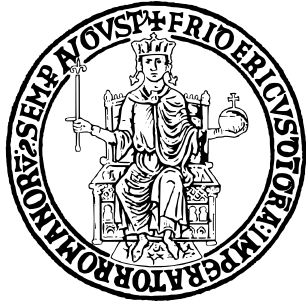


UNIVERSITÀ DEGLI STUDI DI NAPOLI FEDERICO II



SCUOLA POLITECNICA E DELLE SCIENZE DI BASE

DIPARTIMENTO DI INGEGNERIA ELETTRICA E TECNOLOGIE DELL'INFORMAZIONE

FIELD AND SERVICE ROBOTICS

HOMEWORK 4

Professor:
Fabio Ruggiero

Candidate:
Roberto Rocco P38000274

GitHub Repository: <https://github.com/Roberto260?tab=repositories>

Exercise n. 1

Buoyancy is the force exerted by a fluid that opposes the weight of an (partially) immersed object. This force arises due to the pressure difference exerted by the fluid on the object: since pressure increases with depth, the bottom part of the body experiences a greater pressure than the top, resulting in a net upward force. The magnitude of this force is proportional to the fluid density ρ and the volume of displaced fluid Δ , and is given by the formula $b = \rho\Delta g$, where g is the gravitational constant.

In the dynamic model of an underwater robot, the buoyancy force and the gravitational force must both be considered. When these forces are expressed in the body-fixed frame through the rotation matrix R_b , they are given by:

$$\mathbf{f}_g^b = R_b^\top \begin{bmatrix} 0 \\ 0 \\ mg \end{bmatrix}, \quad \mathbf{f}_b^b = -R_b^\top \begin{bmatrix} 0 \\ 0 \\ \rho\Delta g \end{bmatrix}$$

An important aspect to highlight is that these forces act at two distinct points on the body: the center of mass and the center of buoyancy, respectively. Since they are applied at different locations, a torque may be generated. By taking the origin of the body frame at the center of mass, the wrench due to gravity and buoyancy in the body-fixed frame is:

$$\mathbf{g}_{rb}^b = - \begin{bmatrix} \mathbf{f}_g^b + \mathbf{f}_b^b \\ S(\mathbf{r}_b^b)\mathbf{f}_b^b \end{bmatrix}$$

where \mathbf{r}_b^b is the position vector of the center of buoyancy expressed in the body frame, and $S(\cdot)$ denotes the skew-symmetric operator associated with the cross product.

It is important to note that the buoyancy effect is typically neglected in aerial robotics. This becomes immediately clear when examining the buoyancy formula. Although the buoyancy force is present in aerial applications as well, in this case it is proportional to the density of air, which is the surrounding fluid. Since water is approximately 800 times denser than air, the buoyant force experienced by an aerial robot (such as a drone) is about 800 times smaller than that experienced by an underwater robot of the same volume. For this reason, the buoyancy force in aerial systems is negligible when compared to the magnitude of other forces acting on the vehicle.

Exercise n. 2

Statement a: “The added mass effect considers an additional load to the structure.”

Answer: *False.*

The added mass effect is not literally an extra structural mass attached to the body, but a hydrodynamic phenomenon: when the underwater vehicle accelerates, nearby fluid particles must also be accelerated. To accelerate these fluid particles, the body exerts forces upon them, and the fluid exerts equal-and-opposite virtual reaction forces on the body. When a body accelerates, decelerates, or changes its direction while moving in a fluid, it behaves as if it had more mass than it really does, in such a way that, for the forces that are apparently being applied to it, the resulting accelerations are lower than expected.

Statement b: “The added mass effect is considered in underwater robotics since the density of the underwater robot is comparable to the density of the water.”

Answer: *True.*

The added mass effect accounts for the mass of fluid particles accelerated in the fluid domain around the moving vehicle. In the case where the fluid is water, its density is comparable to that of the

underwater robot. Consequently, the virtual reaction forces exerted by the fluid on the body cannot be neglected.

Statement c: “*The damping effect helps in the stability analysis.*”

Answer: *True.*

The damping effect arises from the viscosity of the fluid surrounding the underwater robot. Although often simplified in dynamic models, it is typically represented as a quadratic velocity term multiplied by a positive definite matrix. The energetic contribution of damping is to dissipate the total energy of the system over time. This dissipation is beneficial in stability analysis, as dissipative terms contribute to ensuring system convergence. For instance, in the context of a suitable Lyapunov function, the damping effect appears in the derivative \dot{V} as a negative definite term with respect to the system’s velocity, thus aiding the formal proof of stability.

Statement d: “*The Ocean current is usually considered as constant, and it is better to refer it with respect to the body frame.*”

Answer: *False.*

Ocean current refers to a mass of seawater moving with respect to the surrounding fluid, often differing in properties such as density, salinity, and temperature. Being a natural phenomenon, it is most conveniently expressed in the inertial (world) frame. Moreover, under suitable assumptions, the ocean current can be considered constant and irrotational with respect to this frame. As a result, its velocity can be modeled as:

$$\mathbf{v}_c = [v_{c,x} \quad v_{c,y} \quad v_{c,z} \quad 0 \quad 0 \quad 0]^\top$$

The influence of the ocean current on the dynamics of a rigid body moving in a fluid can be incorporated by introducing the relative velocity between the body and the current. This relative velocity, expressed in the body-fixed frame, is given by:

$$\mathbf{v}_r^b = \mathbf{v}_b^b - R_b^\top \mathbf{v}_c$$

where \mathbf{v}_b^b is the 6-dimensional velocity vector of the robot (linear and angular components) expressed in the body frame, and R_b is the rotation matrix from world to body frame.

The expression of the ocean current velocity in the body-fixed frame is therefore a practical way to incorporate its effect into the dynamic model, which is formulated in the body frame. However, for a proper physical description of the phenomenon itself — and in order to reasonably assume it as constant — the current must be referred to a frame fixed to the Earth. This inertial reference allows the current to be modeled as a steady and irrotational flow, enabling its consistent integration into the vehicle’s equations of motion.

Exercise n. 3

Quadruped Gaits and desired trajectory

The six gaits used in quadruped locomotion are described as follows:

- **Trot (0):** A symmetrical, two-beat gait where diagonal leg pairs (LF+HR and RF+HL) move together. At each moment, two diagonal legs are in stance while the other two swing. This gait is stable and commonly used at moderate speeds.
- **Bound (1):** A symmetrical, two-beat gait in which the hind legs move together, followed by the front legs. Each pair enters stance simultaneously, and the pairs alternate. This gait is typically used for fast, springy movement.
- **Pacing (2):** A two-beat gait where lateral leg pairs (LF+LH and RF+RH) move together. This pattern alternates left and right sides of the body, creating a side-to-side oscillation.
- **Gallop (3):** An asymmetrical, four-beat gait where legs strike the ground one at a time in a specific sequence, typically RH → LH → RF → LF. It is characterized by a fast, dynamic motion with a sequence of individual stances.
- **Trot Run (4):** A faster variant of the trot using the same diagonal leg pairing. Unlike the regular trot, this gait includes a brief aerial phase between each pair's contact, suitable for higher-speed motion.
- **Crawl (5):** A slow, stable, four-beat gait where legs move one at a time in a repeating sequence. Typically, three legs remain in stance while one swings, maximizing balance.

Figure 1 shows the leg contact patterns of the quadruped robot for a 1-second simulation across the six possible gaits. Each row corresponds to a leg, and each column represents time. Green segments indicate periods when the leg is in the *stance* phase, while white segments indicate the *swing* phase. The results shown in the figure were obtained with a desired acceleration of 1 m/s^2 and a desired velocity of 0.5 m/s . Modifying the mass or the friction coefficient in the simulation does not affect the desired leg motion pattern. As a result, the gait diagram remains unchanged under variations of these parameters. Conversely, when varying the desired acceleration and velocity of the robot's trajectory, it is observed that higher velocities require the legs to spend less time in contact with the ground. As a result, the green stance phases within the gait diagrams become thinner, reflecting shorter stance durations.

In Figure 2, the desired trajectory of the robot's Center of Mass (CoM) is analyzed. As shown, the motion starts with a constant acceleration phase ($acc_d = 1$), until the desired velocity ($vel_d = 2$) is reached. After this point, the velocity remains constant. From the plots of position and velocity, it is clear that the walking direction lies along the x -axis, as this is the only component different from zero. The robot's orientation remains constant throughout the motion. The plot displaying the desired z -component of the Ground Reaction Forces (GRFs) has not been included, as it does not offer particularly clear or valuable insight. It is sufficient to observe that the robot's weight, calculated as $m \cdot g$, is evenly distributed among the legs in contact with the ground. The stance pattern, which varies according to the chosen gait, is more effectively interpreted through the gait diagram presented previously. Figure 2 remains invariant with respect to the selected gait. The only effect of changing the gait is a variation in the temporal distribution of the Ground Reaction Forces (GRFs) on the stance legs. To properly run matlab files, give a look at *Readme2.txt* file in the folder.

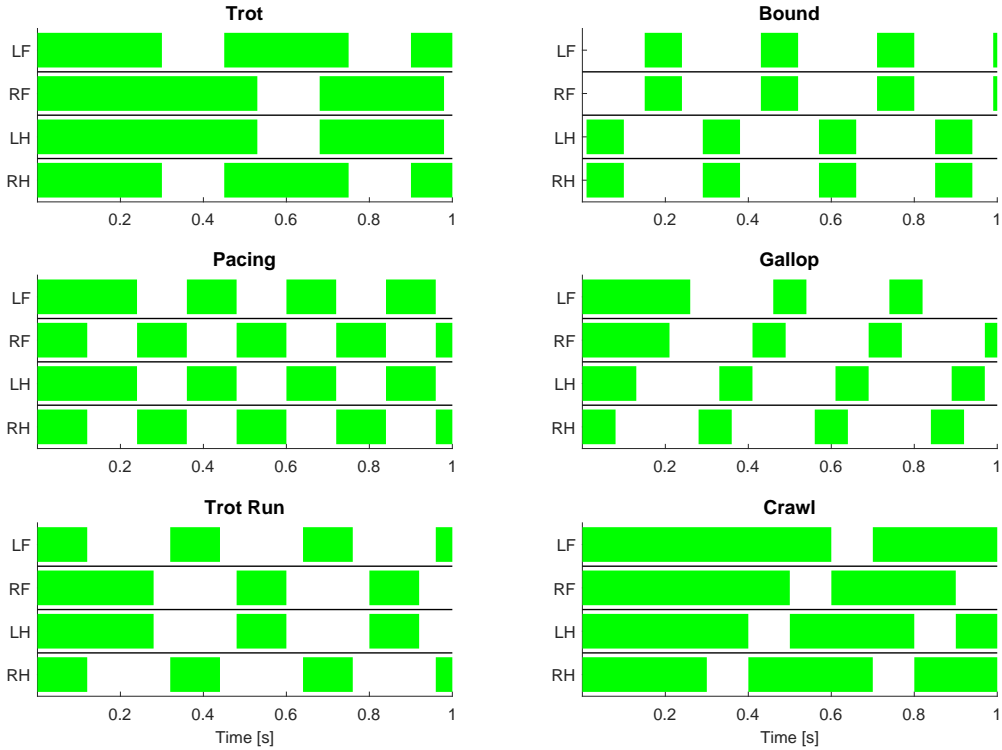


Figure 1: Comparison of All Six Gaits

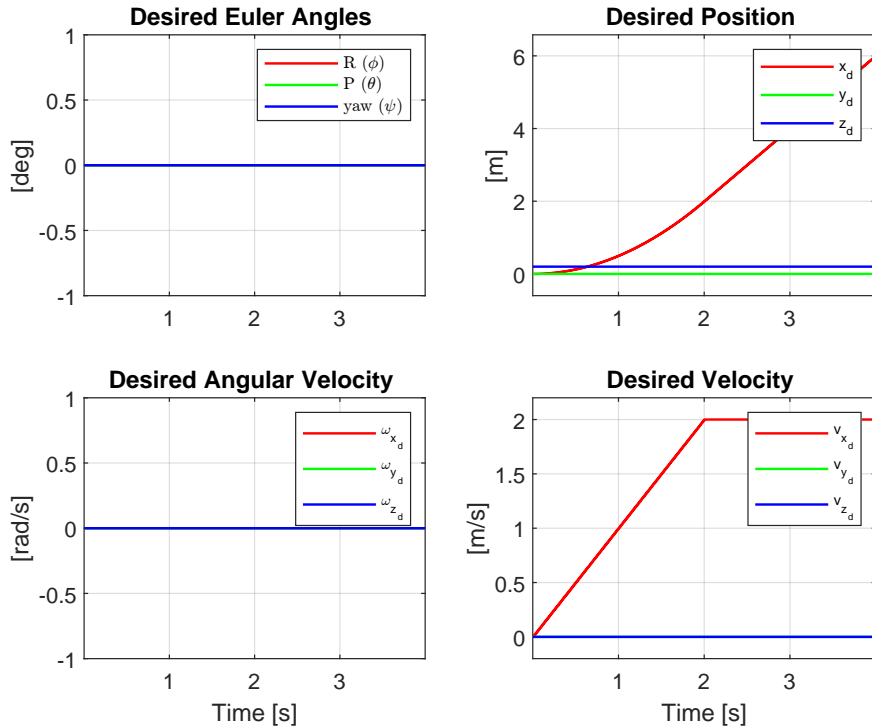


Figure 2: Desired Trajectory

Performance Analysis of different Quadrupedal Gaits

To compare the performance of different quadruped gaits, a desired trajectory was defined with an acceleration $a_d = 1$ and a target speed $v_d = 1.5$. The robot parameters are a mass of $m = 5.5$ and a friction coefficient $\mu = 1$. According to the Froude number (Fr), this motion corresponds to a running regime, since

for a leg length $l = 0.14$, we obtain:

$$\text{Fr} = \frac{v_d^2}{g l} = \frac{(1.5)^2}{9.81 \times 0.14} \approx 1.6.$$

indicating a running regime with likely aerial phases. By looking at the following plots, one can observe that:

Trot: The trot exhibits a moderate longitudinal drift (≈ 0.4) over the run, with small lateral (e_y) and vertical (e_z) oscillations. Angular and angular-velocity errors remain relatively low due to diagonal symmetry in footfall. GRF profiles show alternating diagonal pairs with similar, regular peaks and a moderate duty factor. This symmetry reduces transverse and longitudinal oscillations, containing attitude error and yielding a balance between stability and speed.

Bound: The bound shows larger longitudinal drift (≈ 0.6) and more pronounced oscillations in lateral and vertical errors. Pitch error is higher and angular-velocity spikes occur at transitions between fore and hind support. GRF profiles feature two large impacts (hind then fore) with higher peaks and lower duty factor. The larger vertical center-of-mass excursion and support concentrated at discrete instants increase instability, demanding stronger control effort to limit trajectory deviation.

Pacing: Pacing yields intermediate longitudinal drift (≈ 0.3) but noticeable lateral oscillations and elevated roll and yaw oscillations symmetric around zero. GRF patterns reveal clear lateral impact peaks per leg due to synchronous ipsilateral limb motion. This same-side pairing amplifies lateral coupling and reduces robustness to side perturbations, making precise tracking more challenging than trot while still less extreme than bound.

Gallop: The gallop produces the largest longitudinal drift (≈ 1.0) with significant lateral and vertical oscillations. Yaw error can reach around -60° , indicating major trajectory deviation. GRF sequences show sequential foot contacts and asymmetric loading patterns. The aerial phase and asymmetric sequencing amplify sensitivity to timing and ground-reaction variations, challenging precise tracking despite high forward speed.

Trot Run: Trot run reduces longitudinal drift (≈ 0.15) compared to pure trot but introduces slightly larger lateral and vertical oscillations. Angular errors resemble trot but are less regular due to stronger vertical accelerations, and GRF peaks become sharper and more pronounced. Partial aerial support improves longitudinal tracking but requires tighter control to contain oscillations, reflecting a compromise between stability and dynamic performance.

Crawl: Although not a true run, crawl shows minimal longitudinal drift (≈ 0.06) and very low roll/yaw errors; pitch error is moderate as the robot shifts weight at each step. GRF peaks are evenly distributed with controlled magnitudes. The static-support nature maximizes stability, though pitch adjustments occur during running attempts. This gait yields the best tracking precision but sacrifices dynamic performance.

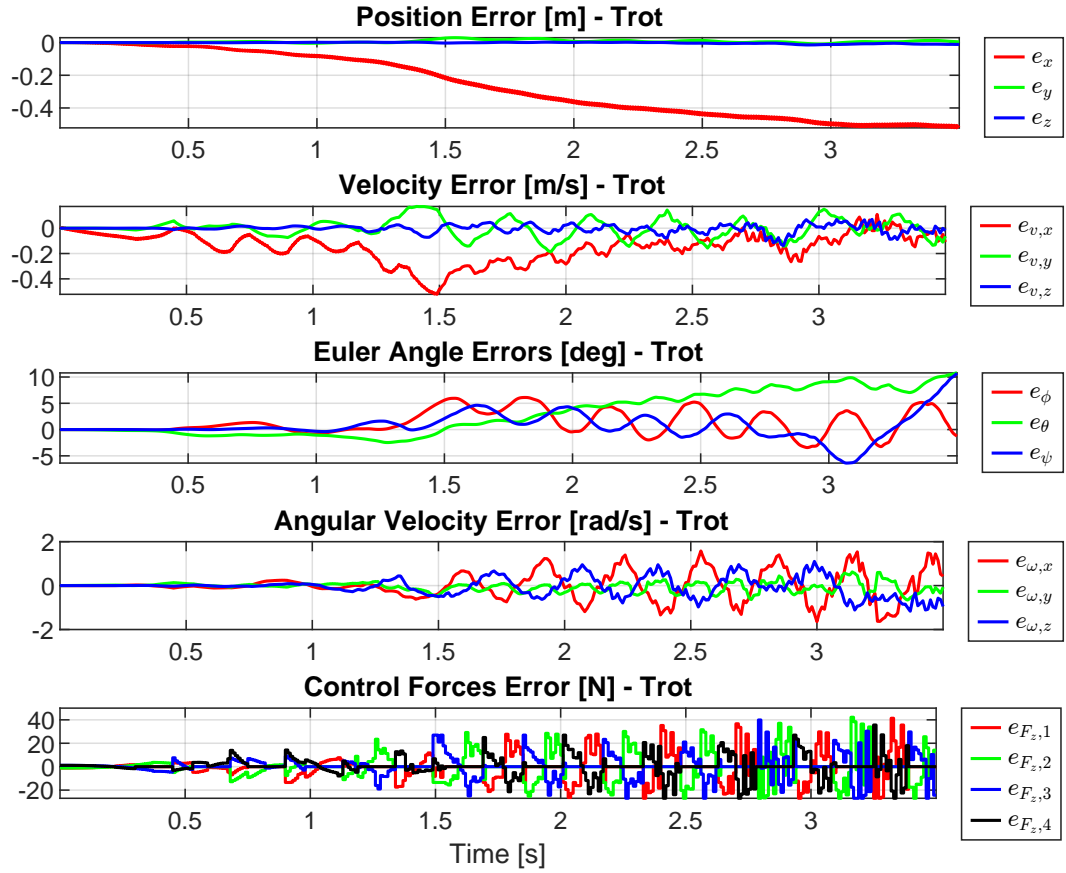


Figure 3: Trot errors evolution

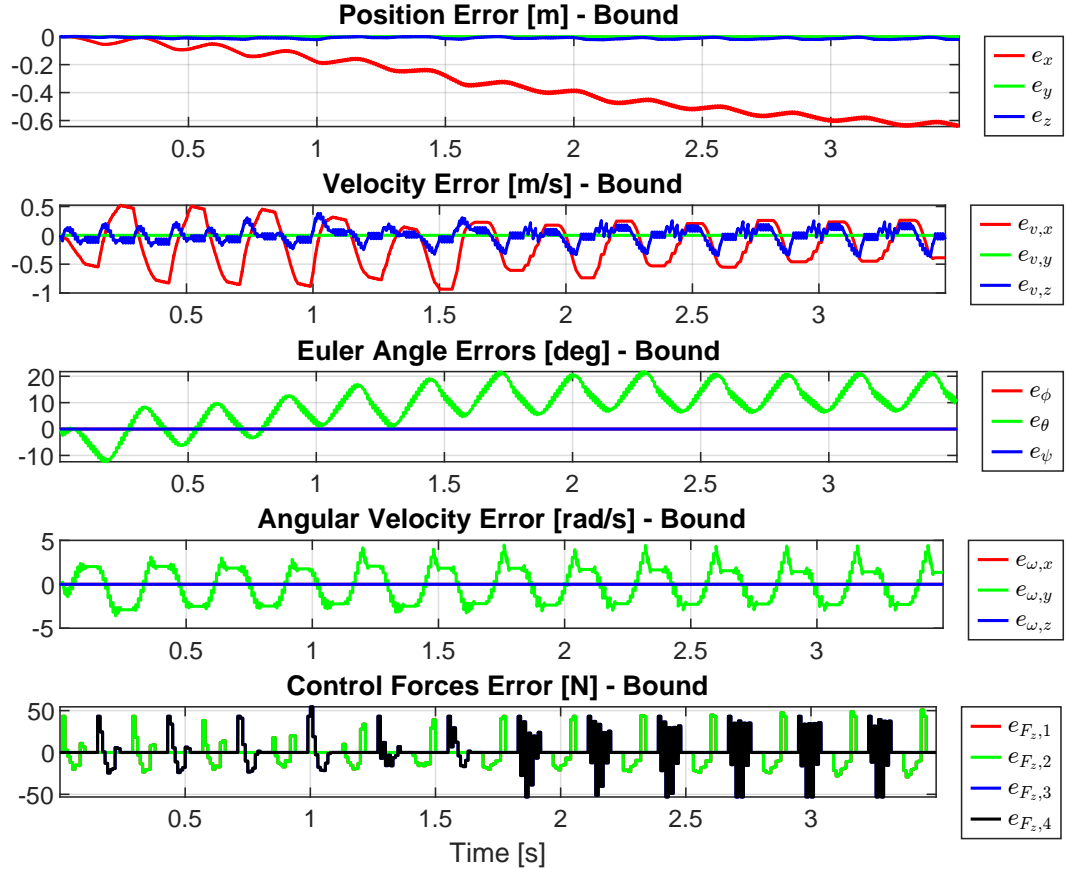


Figure 4: Bound errors evolution

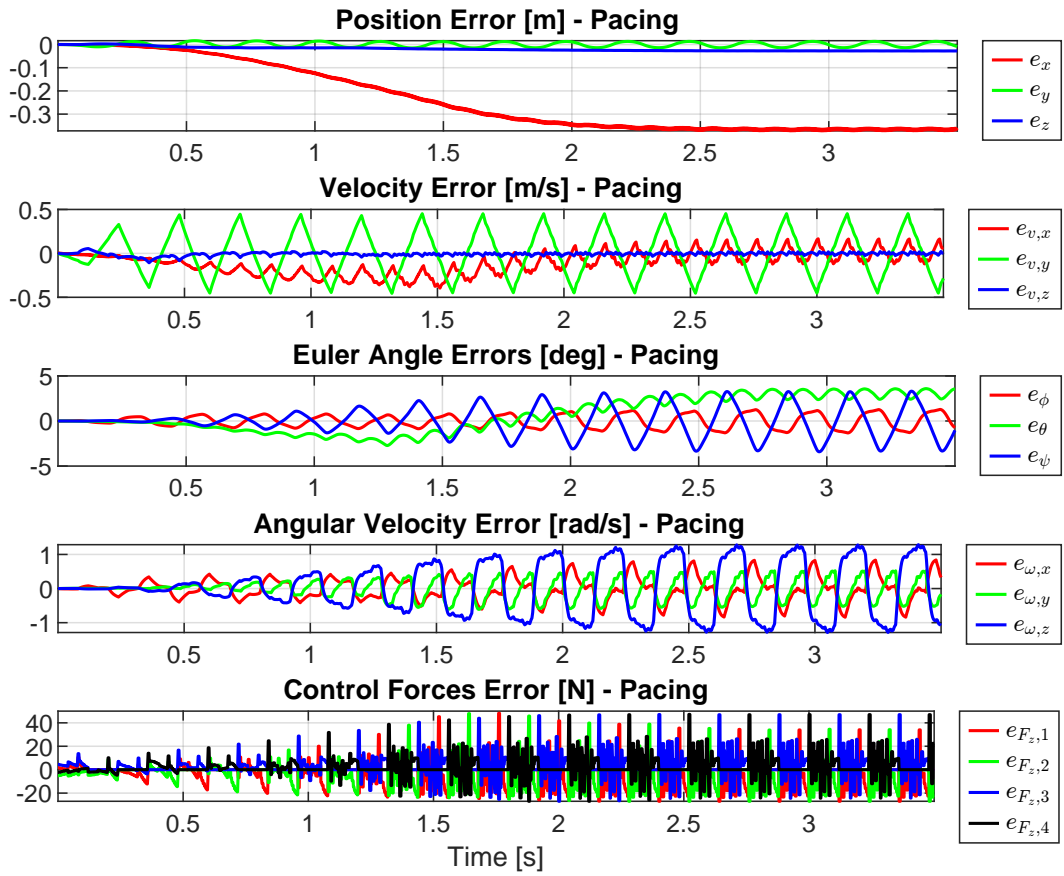


Figure 5: Pacing errors evolution

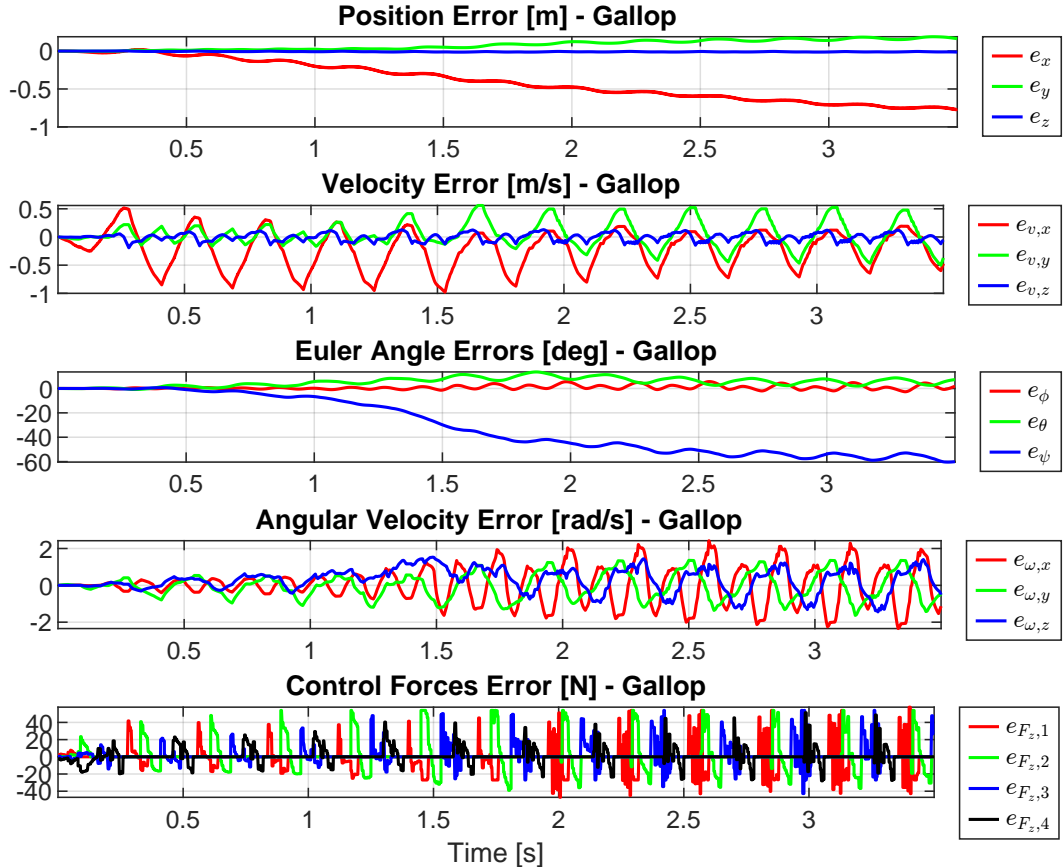


Figure 6: Gallop errors evolution

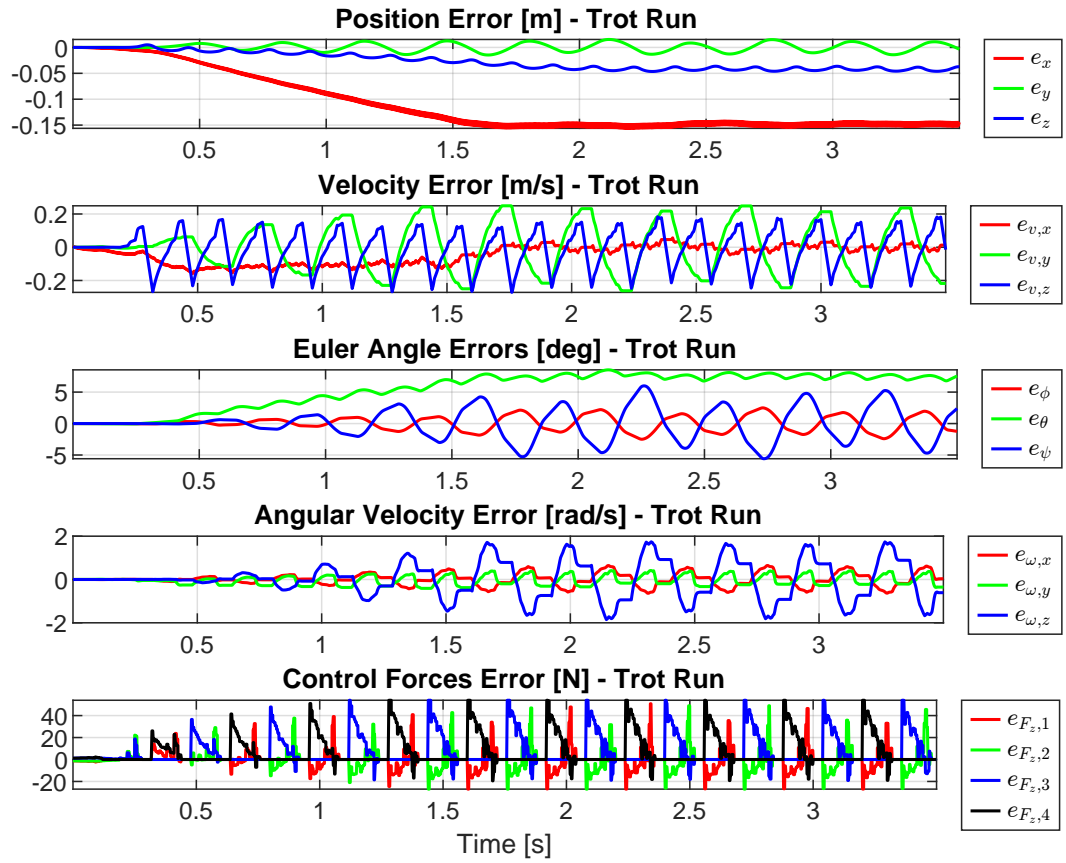


Figure 7: Trot-Run errors evolution

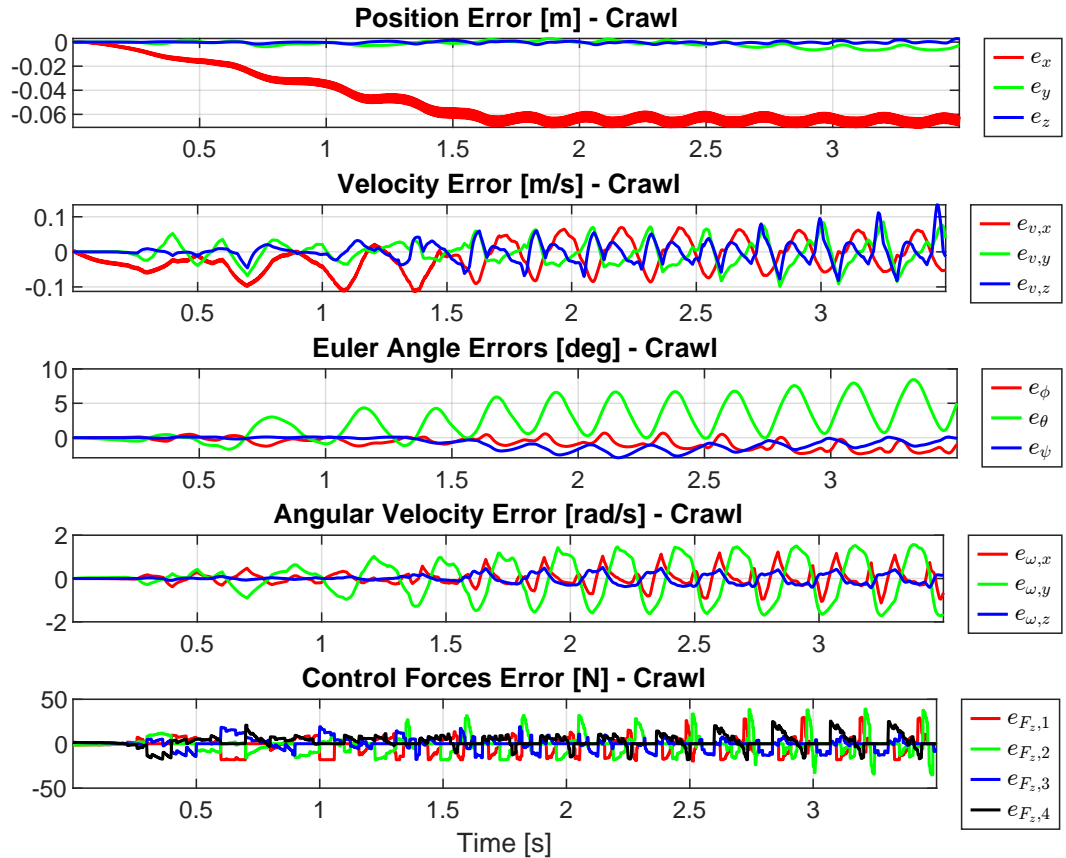


Figure 8: Crawl errors evolution

To summarize, at $\text{Fr} \approx 1.6$, dynamic gaits (bound, gallop) incur higher position and angular errors and pronounced GRF peaks, while conservative gaits (trot run, trot, crawl) achieve lower drift and oscillations at reduced dynamic performance.

From now on different tests will be carried out: modifying mass, friction coefficient, velocity and acceleration, the dynamic characteristics of the gaits that resulted in the poorest tracking performance will be highlighted.

Run test

To test the run performance, a desired trajectory was defined with an acceleration $a_d = 1$ and a target speed $v_d = 2.5$. The robot parameters are a mass of $m = 5.5$ and a friction coefficient $\mu = 5$.

Compared to the previous case, a faster trajectory is desired. To achieve this, the friction coefficient has been increased, allowing the legs to generate more thrust before slipping, thus making the trajectory feasible. As shown in the generated and uploaded video, the resulting trajectory is not feasible for all gaits: **bound** and **trot** result in failure, with the robot collapsing to the ground, while **gallop** follows the trajectory poorly. Among the remaining three gaits, **crawl** minimizes the position error (around -0.1), at the cost of a significant pitch angle error (with peaks up to 20°). While **crawl** sacrifices only the pitch error and maintains negligible errors in the other angular components, **pacing** yields more balanced performance, with a position error on the order of 0.6 . Regarding the linear velocity error, notice the peaks in the y -component during **pacing**; this is due to the simultaneous movement of two legs at a time. Comparing the performance in this case with that of the trajectory implemented in the previous section, a general degradation can be observed, with errors that are overall amplified.

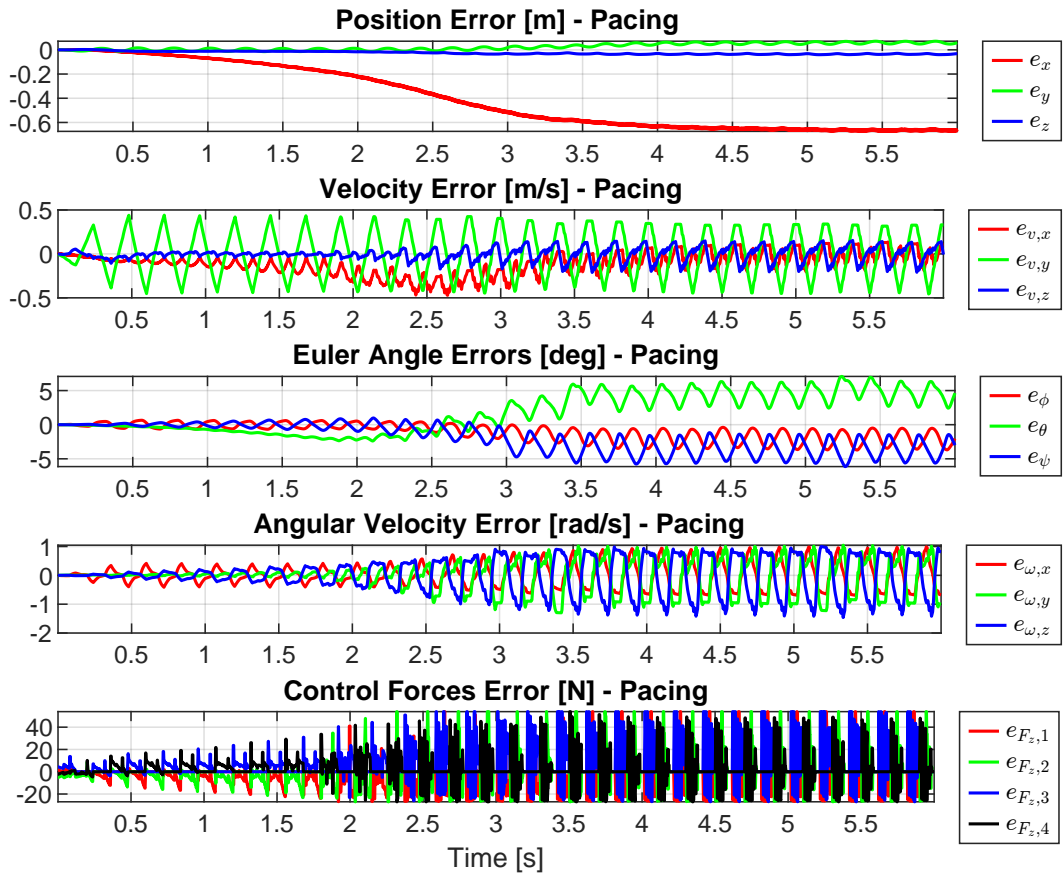


Figure 9: Pacing errors evolution while running

Run test with lighter robot

By modifying the robot's mass, according to the selected gait the performance varies significantly. In particular, reducing the mass generally leads to lower oscillations. Setting the mass to $m = 1.5\text{ kg}$ while maintaining the trajectory used in the run test, both **gallop** and **crawl** show improvements in terms of

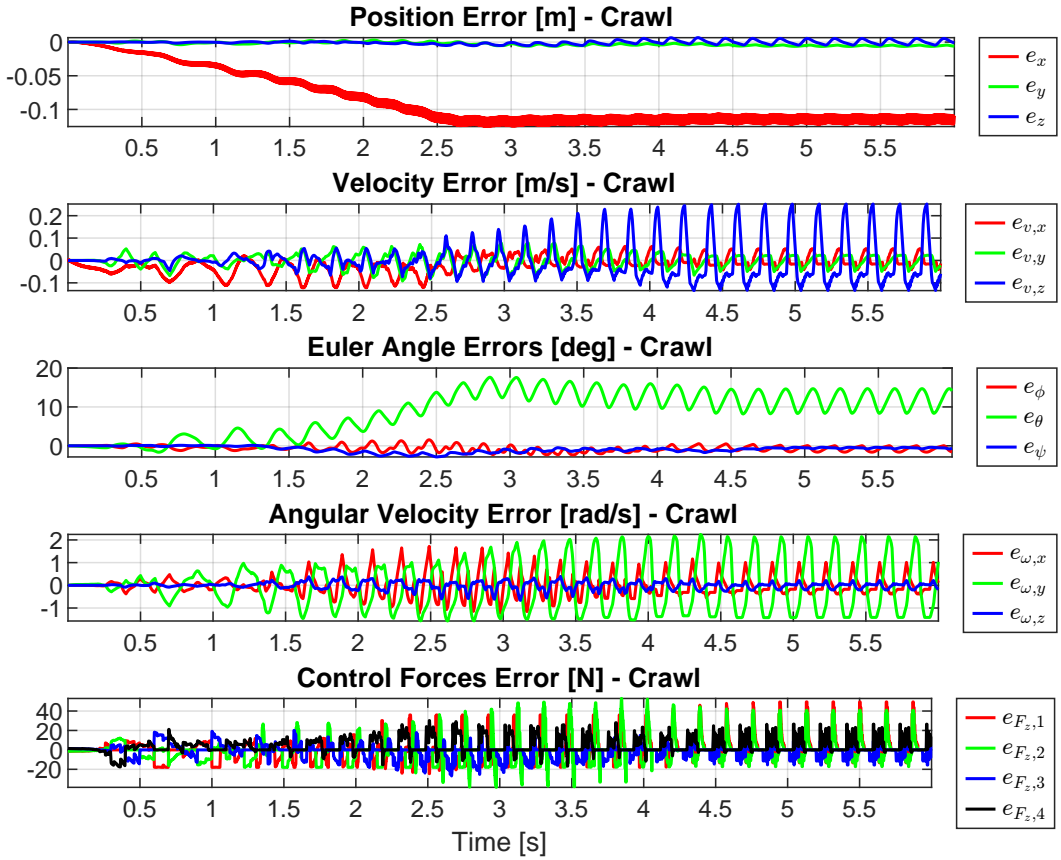


Figure 10: Crawl errors evolution while running

pitch angle error oscillations. A lower mass results in greater stability, as the legs are able to support the weight without excessive flexing. Indeed, in both cases, the amplitude of the pitch error is reduced by half. Below, only the plot for the **pacing** gait is reported; in this case, a noticeable improvement in the linear error is also observed. **Pacing**, which inherently introduces imbalance due to the simultaneous movement of legs on the same side (left/right), shows improved performance when the robot's weight is reduced. Time convergence is reduced. Finally, **gallop** also benefits from the reduced mass: with less weight to carry, the quadruped is better able to follow the reference trajectory. In the final moments, a decreasing trend in the error is observed, as shown in the plot.

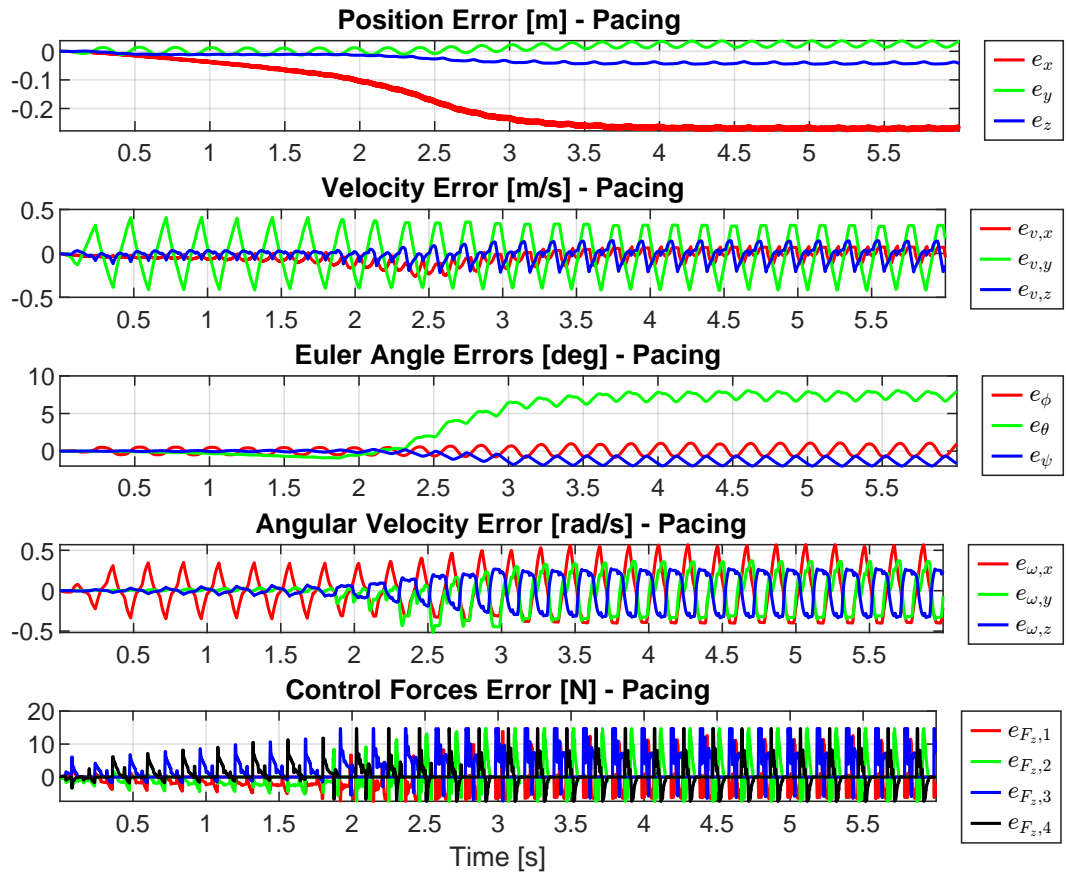


Figure 11: Pacing errors evolution while running, with $m = 1.5 \text{ kg}$

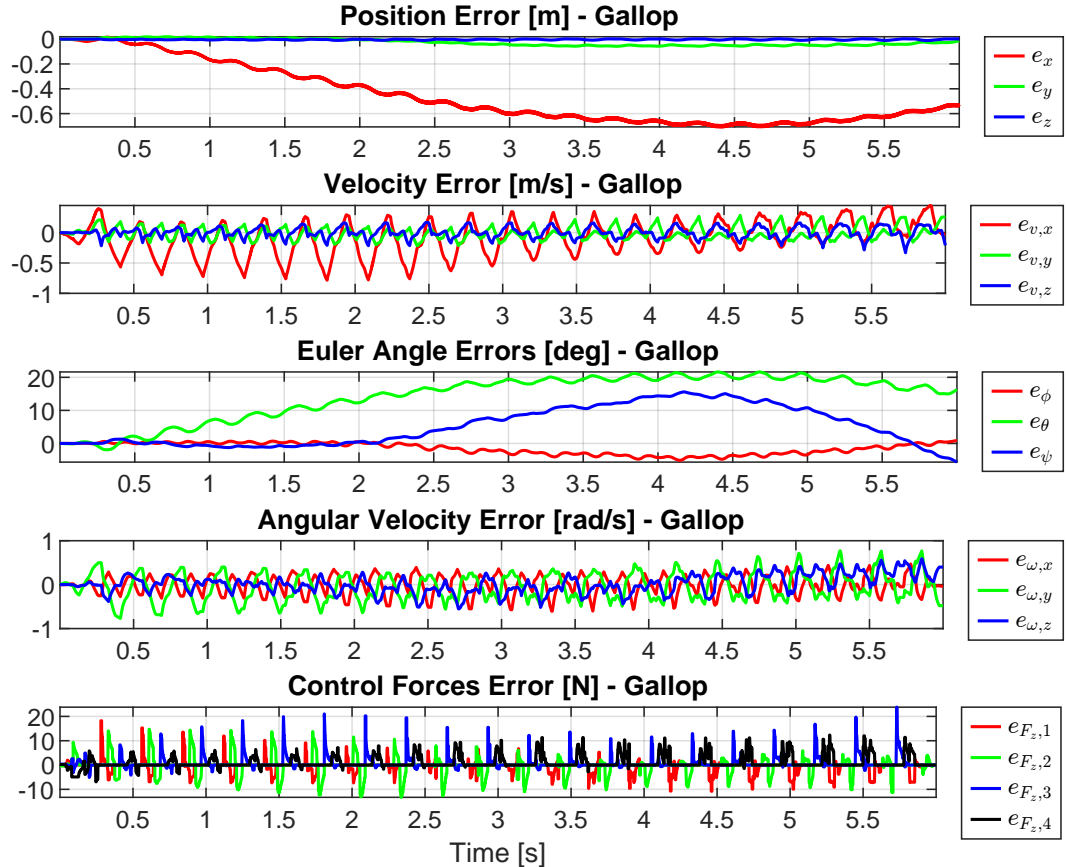


Figure 12: Gallop errors evolution while running, with $m = 1.5 \text{ kg}$

Run test with smaller friction coefficient

By modifying the friction coefficient, according to the selected gait the performance varies significantly. For this test, the trajectory from the run test was selected, with a friction coefficient set to $\mu = 1.2$ and a mass of $m = 5.5\text{ kg}$. Running the simulation reveals a general degradation in performance, and further reducing the coefficient makes some gaits infeasible. Below, the results for the `crawl` gait are reported. As shown, the convergence of the position error is significantly slower compared to the original case and settles at a worse value. The same observation holds for the orientation error. This highlights the importance of having a sufficiently high surface friction coefficient; otherwise, the robot tends to slip and is unable to generate adequate ground reaction forces (GRFs). In fact, the x and y components of the GRF decrease as μ decreases. Conversely, increasing the friction coefficient does not significantly alter the performance for trajectories that are already feasible.

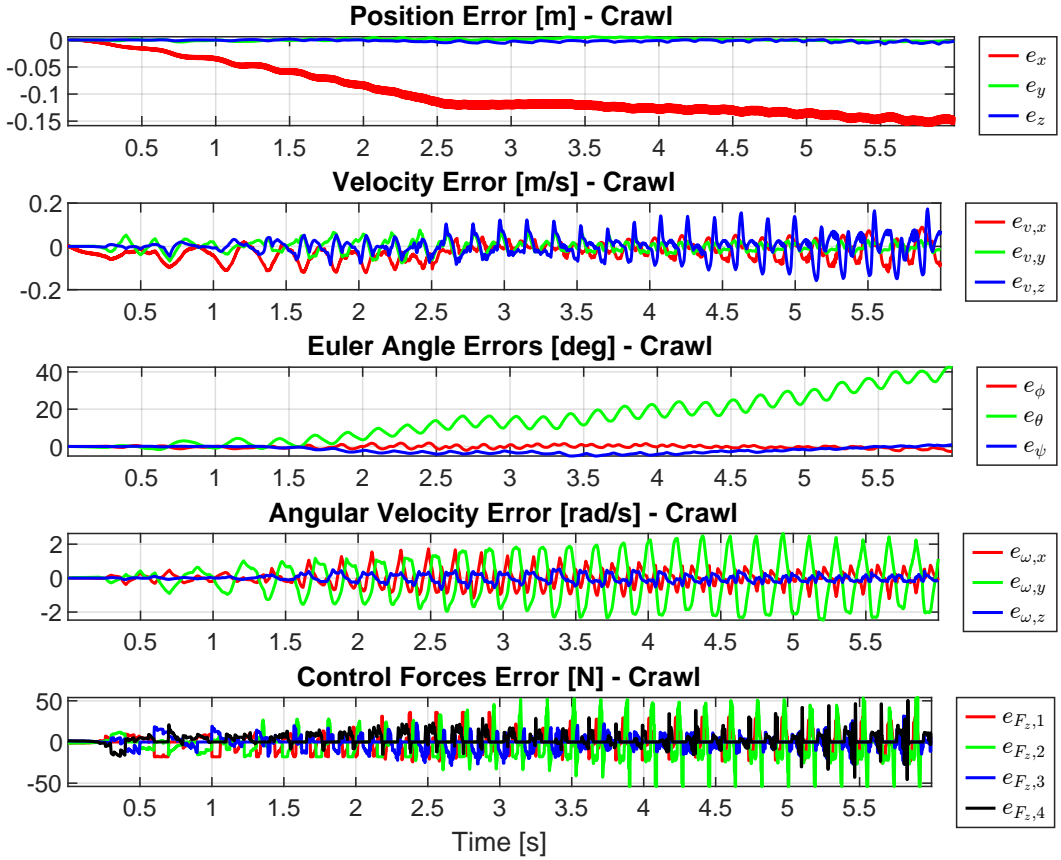


Figure 13: Crawl errors evolution while running, with $\mu = 1.2$

Exercise n. 4

The rimless wheel model is used to represent the passive walking behavior of a biped. We consider the following parameters:

$$g = 9.81 \text{ m/s}^2, \quad l = 1 \text{ m} \quad (\text{leg length}), \quad \alpha = \frac{\pi}{8} \text{ rad} \quad (\text{half inter-leg angle}), \quad \gamma = 0.08 \text{ rad} \quad (\text{slope angle}).$$

The dynamic model in the single-support phase is given by

$$\ddot{\theta} = \frac{g}{l} \sin(\theta), \quad \text{with starting condition } \theta(0^+) = \gamma - \alpha.$$

that is, system starts immediately after a leg exchange. It is important to recall that each time the wheel reaches a configuration satisfying the double support condition, a discrete jump occurs in the state variables: the angular velocity is updated according to the conservation of angular momentum with respect to the contact point, while the angular position by changing the reference with respect to θ is defined. Under these conditions, system behavior can be studied by modifying the initial velocity. It is observed that:

- For $\dot{\theta}_0 > 0$, forward walking occurs if $\dot{\theta}_0 > \omega_1$, where

$$\omega_1 = \sqrt{2 \cdot \frac{g}{l} (1 - \cos(\gamma - \alpha))} \approx 0.97542 \text{ rad/s.}$$

When this condition is satisfied, passive walking begins and the system converges to a stable limit cycle characterized by periodic oscillations in θ . For $0 < \dot{\theta}_0 < \omega_1$, the system instead converges to a stable equilibrium where $\dot{\theta} = 0$ and $\theta = \gamma \pm \alpha$, which corresponds to approximately -0.312 rad and 0.472 rad. These equilibria are physically equivalent, both representing the static double support configuration.

Thus, the basin of attraction of the limit cycle is defined by initial conditions $\dot{\theta}_0 > \omega_1$, while the equilibrium is reached for $0 < \dot{\theta}_0 < \omega_1$. An example of trajectory is showed in Fig.14.

- For $\dot{\theta}_0 < 0$, the biped attempts to walk uphill in the starting phase. In this case, the system exhibits irregular behavior, and it becomes difficult to clearly define the basins of attraction for either the limit cycle or the equilibrium. The convergence to either the limit cycle or the equilibrium is determined by the last negative velocity attained by the wheel before the direction of motion reverses. Specifically, at a certain point, the upward motion is halted and reversed due to the effect of gravity. A "step" initially taken uphill with a negative initial velocity $\dot{\theta}_0^-$ fails to be completed. From that instant onward, the motion becomes a descent, starting from an angular position θ_0 that depends on the previous $\dot{\theta}_0^-$.

It is observed that if θ_0 is sufficiently close to zero, the wheel is able to accumulate enough energy during the descent to sustain forward walking, ultimately leading to convergence to a limit cycle. This condition occurs for values of $\dot{\theta}_0^-$ in the interval $[-1.38, -1.46]$, while for smaller value convergence to the (previous) equilibrium is ensured. The issue with higher negative initial velocities is that they enable the wheel to complete the step in the backward direction. To determine the conditions for convergence to a limit cycle, one must identify the initial angular velocities $\dot{\theta}_0$ such that the last incomplete "step" in the uphill direction occurs with an initial velocity within the aforementioned interval.

To find such initial velocities, it is sufficient to recall that the initial velocity of a step is related to the final velocity of the previous step by the formula:

$$\dot{\theta}^+ = \cos(2\alpha) \cdot \dot{\theta}^-,$$

where $\dot{\theta}^-$ is the angular velocity immediately before impact, and $\dot{\theta}^+$ is the velocity just after the impact due to a leg exchange.

Moreover, the final velocity of a step (i.e., just before the next impact) is related to the initial velocity of that step (i.e., just after the previous impact) by the expression:

$$\dot{\theta}(t^-) = \sqrt{\dot{\theta}^2(0^+) + 4\frac{g}{l} \sin \alpha \sin \gamma}.$$

This relationship provides a way to recursively compute the angular velocity from one step to the next and to determine whether the system converges to a limit cycle. Plots in Fig.15 shows different behavior, while motion inversion can be appreciated in both cases.

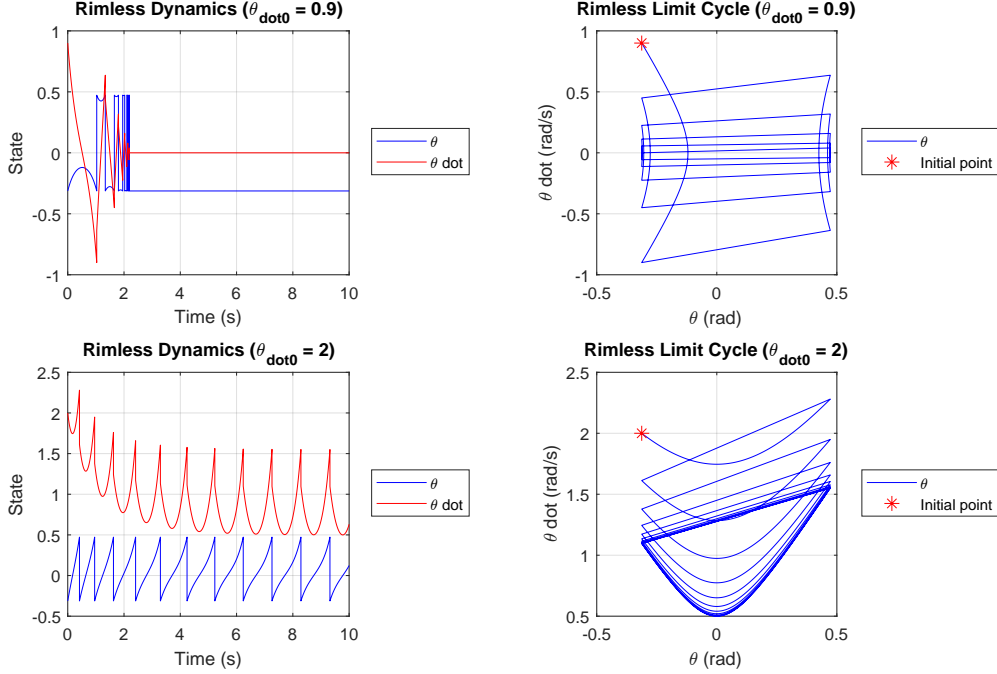


Figure 14: Comparison of rimless dynamic and phase portrait

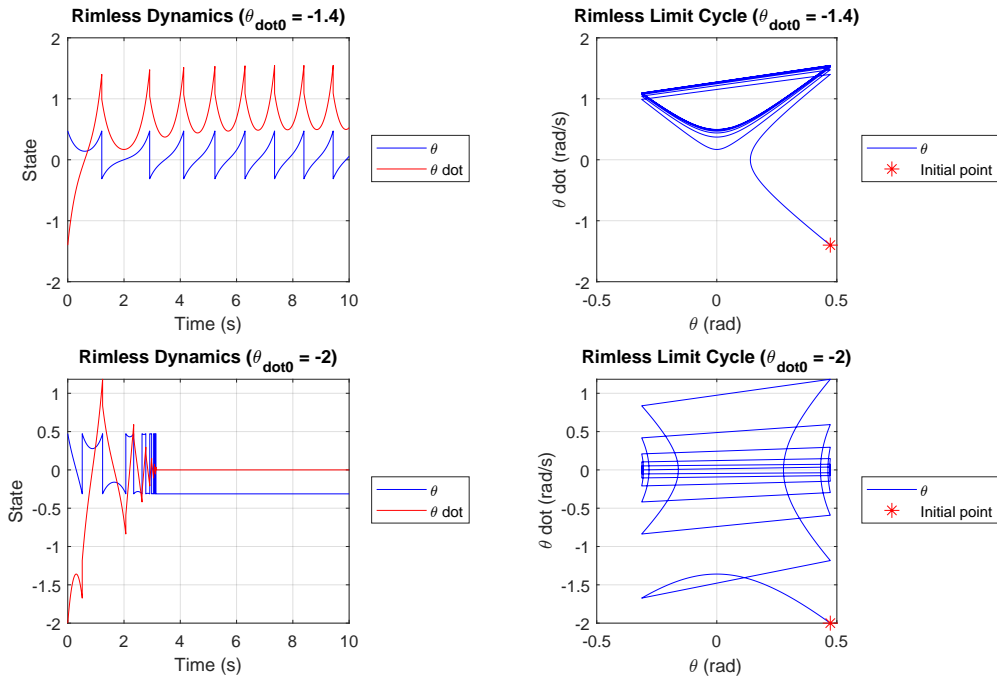


Figure 15: Comparison of rimless dynamic and phase portrait

Finally, by modifying the parameters initially defined, it is possible to observe changes in the shape of the limit cycle, the equilibria to which the system converges, as well as in the convergence threshold ω_1 . Consequently, the previously defined intervals corresponding to the basins of attraction are also affected. Fixing the initial angular velocity fixed at 0.95 rad/s, one can invert the formula for ω_1 previously defined, in order to find condition on parameters that ensure convergence to limit cycle or equilibrium. For example, by inverting the condition for the onset of forward walking, one finds that choosing the leg length atleast equal to

$$l_{\min} = \frac{2g(1 - \cos(\gamma - \alpha))}{0.95^2} = 1.0542$$

results in convergence to a limit cycle; otherwise, the system will converge to the equilibrium. It is worth noting that this constitutes a bifurcation analysis with respect to the parameter l . By changing l in the limit cycle interval, you can modify its shape, while the equilibrium remains unperturbed. For the angles α and γ , the same inversion approach cannot be applied due to complications arising from the inverse cosine function. A more practical method is to distinguish between different cases:

1. If $\gamma > \alpha$, the system will certainly exhibit a limit cycle. In particular, the mass is always ahead of the stance foot, and the standing fixed point disappears. Under this condition, no equilibria are present, and the limit cycle becomes globally attractive.
2. If $\gamma = \alpha$, the prescribed velocity 0.95 is sufficient to ensure convergence to a limit cycle, as any positive initial velocity will initiate forward walking.
3. If $\gamma < \alpha$, one must substitute the given values into the expression for ω_1 and verify whether the previously stated condition for the onset of the limit cycle is satisfied.

Both angles α and γ influence the steady-state behavior of the system—whether it converges to an equilibrium or a limit cycle—as well as the specific equilibrium reached and the shape of the limit cycle.

The equilibrium points are always given by: $(\theta, \dot{\theta}) = (\gamma \pm \alpha, 0)$.

Regarding the limit cycles, a decrease in α leads to more frequent resets, resulting in a limit cycle with higher frequency. Conversely, an increase in γ corresponds to a steeper slope, which induces higher speeds and thus more frequent resets as well. In Fig 16, it is possible to appreciate how different γ change the number of oscillation achieved in the same time by the wheel, and consequently the shape of the stable limit cycle

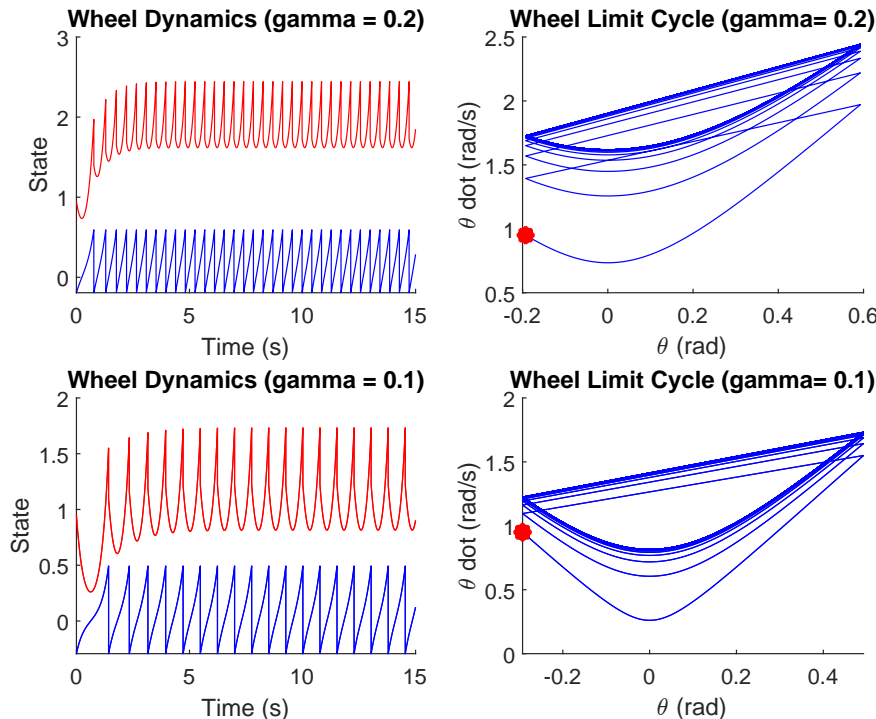


Figure 16: Comparison of rimless dynamic and phase portrait with different γ